CCS Chemistry

# IMMEDIATE ONLINE ACCEPTED (IOA) ARTICLE



*IOA Posting Date: April 11, 2024*

TITLE: Tailored Interphases Construction for Enhanced Si Anode and Ni-Rich Cathode Performance in Lithium-Ion Batteries

AUTHORS: Yuxiang Huang, Yuchen Ji, Guorui Zheng, Hongbin Cao, Haoyu Xue, Xiangming Yao, Lu Wang, Shiming Chen, Zuwei Yin, Feng Pan and Luyi Yang

DOI: 10.31635/ccschem.024.202404120

CITE THIS: *CCS Chem.* **2024**, Just Accepted. DOI: 10.31635/ccschem.024.202404120

# Tailored Interphases Construction for Enhanced Si Anode and Ni-Rich Cathode Performance in Lithium-Ion Batteries

Yuxiang Huang[1,4], Yuchen Ji[1,4], Guorui Zheng[2,*], Hongbin Cao[1], Haoyu Xue[1], Xiangming Yao[1], Lu Wang[1], Shiming Chen[1], Zuwei Yin[3], Feng Pan[1,*] and Luyi Yang[1,*].

[1] School of Advanced Materials, Peking University Shenzhen Graduate School, Shenzhen, 518055.
[2] Institute of Materials Research (IMR), Tsinghua Shenzhen International Graduate School, Tsinghua University, Shenzhen 518055.
[3] College of Energy, Xiamen University, Xiamen 361005.
[4] These authors contributed equally to this work.
* Corresponding author E-mail: zhengguorui1991@163.com (G. Z.); panfeng@pkusz.edu.cn (F. P.); yangly@pkusz.edu.cn (L. Y.);

## Abstract

As promising candidates for high-energy-density lithium-ion batteries, both silicon (Si) anodes and nickel-rich cathodes face significant challenges due to structural instability arising from interphases. In this study, we introduce tetravinylsilane (TVSi) as a multifunctional electrolyte additive to engineer tailored interphases simultaneously on Si anode and $LiNi_{0.92}Mn_{0.05}Co_{0.03}O_2$ cathode, thereby enhancing their electrochemical performance. On one front, TVSi undergoes polymerization, leading to the formation of a composite solid electrolyte interphase (SEI) with an interpenetrating network structure on the Si surface. This SEI effectively accommodates the volume changes during cycling, inhibiting SEI growth and thereby preserving the capacity. On the other front, the TVSi-induced cathode-electrolyte interphase (CEI) exhibits a dense structure comprising a chemically bonded silicate-silane polymer. This CEI effectively mitigates transition metal dissolution by scavenging hydrofluoric acid and reduces irreversible phase transitions by minimizing side reactions. As a result of the enhanced interfacial stability achieved on both electrodes, TVSi enables improved performance in full cells with a $LiNi_{0.92}Mn_{0.05}Co_{0.03}O_2$ cathode paired with a silicon anode. This multifunctional additive strategy offers a novel perspective on additive design for high-energy-density lithium-ion batteries, showcasing its potential for advancing battery technology.

**Keywords:** electrolyte additive; solid electrolyte interphase; cathode electrolyte interphase; in situ interface characterization; lithium-ion battery

## 1.Introduction

The increasing demand of portable energy storage has promoted the development of lithium-ion batteries toward cheaper price, higher energy density and longer lifespan. In this respect, silicon (Si) has become the promising candidate of anode due to its high theoretical capacity, low working plateau and abundant resource.[1, 2] For the cathode candidates, high-nickel (Ni) layered oxide $LiNi_xMn_yCo_zO_2$ (x+y+z=1, x>0.9) materials stand out for the higher specific capacity at the same cut-off voltage. [3, 4]Therefore, pairing Ni-rich cathode and Si anode is likely to meet the commercial requirement for high-energy-density lithium-ion batteries.

However, toward their commercialization, a series of issues remain unsolved. For Si anode, the main challenge is the instability of solid-electrolyte interphase (SEI) caused by the continuous Si volume swing.[5, 6] The expansion and shrink can damage the SEI and expose the Si particle surface to the electrolyte, resulting in continuous electrolyte consumption and SEI growth.[7] Fluorinated carbonates, such as FEC, is frequently reported as an effective anode additive,[8-11] owing to its ability to construct a inorganic LiF-rich SEI with higher chemical stability and hardness.[12, 13] However, merely increasing the amount of hard inorganic products is insufficient to form a resilient SEI. As for Ni-rich cathodes, the thermal decomposition or electrochemical oxidation of FEC and lithium hexafluorophosphate ($LiPF_6$) salt can generate various acid (e.g. HF), especially at high voltages,[14-17] which is commonly reported to trigger the transition metal (TM) dissolution, leading structural degradation of Ni-rich cathode materials.[18, 19] Therefore, constructing interphases with superior mechanical and chemical property on both Si anode and Ni-rich cathode is essential to mitigate above interphase-originated issues.[20, 21] One of the key pathways is to *in-situ* modify the interphases via multi-functional electrolyte additive engineering, so that stable CEI and SEI can be simultaneously constructed on cathode and anode, respectively.

Considering the key origins of interfacial instability on Si-based anodes and Ni rich cathodes are different, a wealth of molecular properties (e.g. decomposition voltages and decomposition products) should be taken into consideration for choosing additives. On the surface of silicon anodes, the SEI should exhibit a structure characterized by flexibility and adaptability, complemented by appropriate mechanical strength to accommodate volumetric changes. In contrast, for the cathode surface, a structurally rigid and dense configuration is essential for the CEI to effectively prevent electrolyte penetration and enhance interfacial stability. Therefore,

Herein, tetravinylsilane (TVSi) is proposed as a promising additive due to its unique molecular structure (**Figure 1a**). With four carbon-carbon double bonds and silicon-based structure, TVSi is expected to form crosslinked polymeric species.[22, 23] Additionally, it is reported that silanes serve as HF scavengers in the electrolyte, protecting the phase of Ni-rich cathodes.[24, 25] In this work, 1wt% TVSi is introduced into a commercial electrolyte (1M $LiPF_6$ in EC: EMC = 3: 7 vol% with 10wt% FEC) for high performance nano-Si anode and $LiNi_{0.92}Mn_{0.05}Co_{0.03}O_2$ (Ni92) cathode. Through comprehensive characterizations, coupled with theoretical calculations, the protection mechanisms on Si anodes and Ni-rich cathodes are revealed. On the surface of the Si anode, the polymerization process

forms a SEI with distinctive interpenetrating network structure on Si, featured by rigid inorganic species embedded in a flexible silane polymer framework. This structure enhances the modulus and uniformity of the SEI, enabling it to maintain its integrity during the silicon volume swing and furthermore restricting the SEI growth. On the surface of Ni92, a dense CEI layer featured by covalently bonding organic polymers with inorganic substances structure is generated, which impedes the electrolyte penetration, lessens the interface side reactions and alleviates the irreversible phase transformation. Through constructing chemically and mechanically stable interphases on both sides of the electrodes, the proposed multifunctional additive effectively improves the performance of the full cell.

## 2.Experimental Methods

### 2.1 Electrolytes and Electrode Preparation

The baseline electrolyte is comprised of 1M $LiPF_6$ in EC: EMC = 3: 7 vol% with 10wt% FEC. The experimental group contains an extra 1% wt% TVSi. The anode consists of Si, acetylene black (AB), and polyacrylic acid (PAA) in 3:1:1 (wt%), applied to copper foil. For the cathode, $LiNi_{0.92}Mn_{0.05}Co_{0.03}O_2$, AB, and polyvinylidene fluoride (PVDF) are mixed in an 8:1:1 weight ratio, coated onto aluminum foil.

### 2.2 Cell Assembly and Electrochemical Measurement

All the cells in this work were assembled in CR2032 coin cells. Coin cells are initially activated and continuously charged and discharged (Si: 0.2C = 840 mA/g; Ni92 1C = 200 mA/g) under galvanostatic control at the temperature of 25 °C or 45 ℃. All the electrochemical measurements are carried out by the Neware battery test system. For the EIS test, the cells were monitored in the frequency range from 1MHz to 0.01Hz.

### 2.3 Characterization

Fourier Transform Infrared Spectroscopy (FTIR) was utilized for observing variations in electrolyte components. Atomic Force Microscopy (AFM), X-ray Photoelectron Spectroscopy (XPS), and Time of Flight Secondary Ion Mass Spectrometry (TOFSIMS) were used for analyzing the chemistry and properties of SEI and CEI. Electrochemical Quartz Crystal Microbalance (EQCM), Inductively Coupled Plasma Atomic Emission Spectroscopy (ICP-AES), and Ultraviolet and Visible Spectroscopy (UV-Vis) were utilized for monitoring transition metal variation. Scanning Electron Microscopy (SEM) and Transmission Electron Microscopy (TEM) were used for observing the microstructure of the materials.

### 2.4 Computational Methods

Density Functional Theory (DFT) was used to investigate the reaction mechanisms, analyze molecular orbital energies, and simulate infrared vibrations. Molecular dynamics simulation was

utilized to explore the behavior of electrolyte components. More detailed information can be found in supporting information.

## 3.Result and Discussion

The film-forming capability of TVSi is firstly evaluated through theoretical calculations. The lowest unoccupied molecular orbital (LUMO) and the highest occupied molecular orbital (HOMO) levels of the electrolyte solvents and TVSi are initially calculated to verify the electrochemical redox reaction priority (**Figure 1b**). Compared with other solvents, TVSi exhibits the lowest LUMO energy (-1.05 eV) and the highest HOMO energy (-7.49 eV), indicating that TVSi is the most favourable component for both reduction and oxidation reactions in the electrolyte, hence a suitable sacrificial film-forming agent for both cathodes and anodes. To prove the feasibility of TVSi polymerization reaction on electrodes, density functional theory (DFT) calculations were carried out (**Figure 1c, S1 & S2**), showing that TVSi undergo $F^-$ and $Li^+$ triggered carbon-carbon double bond cleavage reactions on cathode and anode sides, respectively. At anode, the energy of this reaction transition state is 0.47 eV higher than the reactants, which is a relatively low energy barrier, while the energy of the generated radical products is 0.06 eV lower than the reactants. In practical situations, the presence of additional electrical energy is conducive to overcoming the transition state of the reaction. These radicals eventually undergo a radical termination process with other radicals, resulting in a final energy state that is 3.50 eV lower than the combined energy of the two radicals (e.g. Bimolecular termination). Similar results at cathode prove that both reaction processes are thermodynamically and kinetically favourable. These calculations all suggest that TVSi can polymerize *in-situ* on the surface of the electrodes, forming polymer electrodes-electrolyte interphase components to protect the anode and cathode.

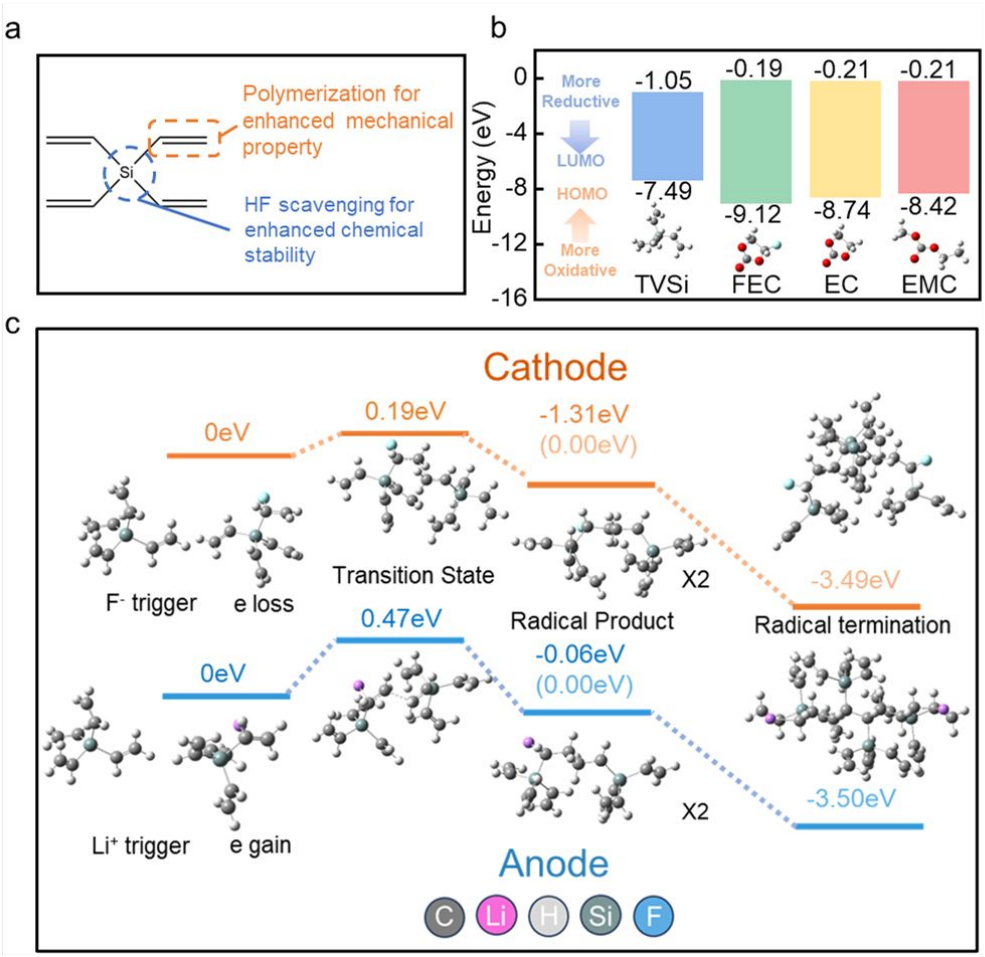


**Figure 1.** (a) Molecular structure design strategy for TVSi additive. (b) The LUMO and HOMO energy levels of TVSi, FEC, EC and EMC. (c) Proposed polymerization processes of TVSi at cathode and anode.

Galvanostatic cycling performance of Si anodes with the baseline electrolyte (denoted as BE) and 1% TVSi containing electrolyte (denoted as BE + 1%TVSi) was evaluated at room temperature (**Figure 2a-b**). Both the electrolytes deliver similar initial specific capacity at 0.2 C after activization. As shown in **Figure S3**, with TVSi, the curve exhibits a slightly prolonged plateau during the initial cycle activation, indicating that TVSi is decomposed and participates in the formation of the SEI during the initial cycle activation. Thanks to the TVSi additive, the specific capacity retention of Si anode greatly increases from 30% to 80% after 300 cycles, with 2281 mAh $g^{-1}$ specific capacity remained. The working voltage of TVSi group in the final cycle maintains 0.31V, while the blank declines to 0.24 V with shorter and more pronounced overpotentials. Compared with BE, a superior rate capability is also achieved by BE + 1%TVSi (**Figure S4a**) owing to the lower impedance (**Figure S5**). The electrochemical performance improvement exhibits more remarkable at harsh operating conditions. With 1% TVSi additive, the capacity retention of the Si anode maintains 70% after 150 cycles at 45℃ (**Figure S4b**). In comparison, due to the accelerated side reactions, the capacity of BE group nearly fades to zero after 150 cycles.

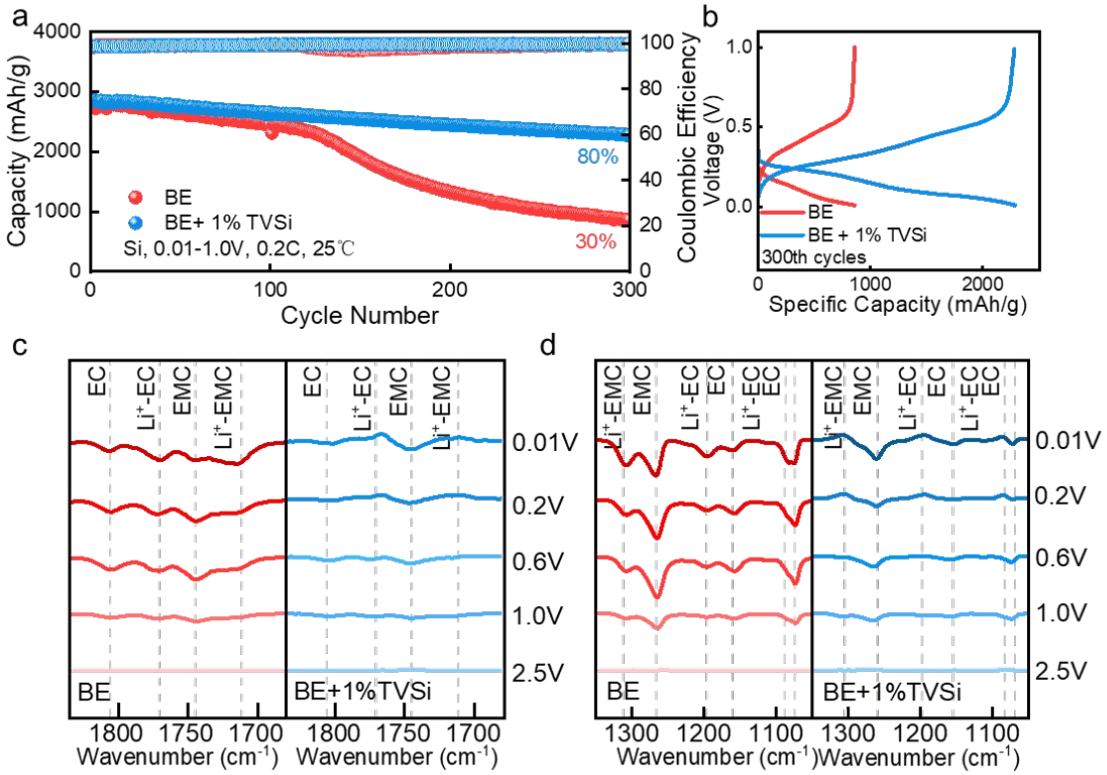


**Figure 2.** Electrochemical performance of Si||Li half cells. (a) Cycle performance at 25℃, (b) capacity-voltage curve at the 300$^{th}$ cycle. *In-situ* FTIR measurement on silicon surface: (c) In-situ FTIR difference spectra within C=O stretching region on Si with BE (in red) and BE + 1% TVSi (in blue), (d) C-O stretching region.

To verify the reduction mechanism of TVSi on silicon anode, the electrolyte environment was initially examined by molecular dynamic (MD) calculation and Fourier transform infrared spectroscopy (FTIR). Differences can be hardly observed in the radial distribution function (RDF) graphs and FTIR spectra between BE and BE + 1%TVSi (**Figure S6 & S7**), revealing that the addition of TVSi barely influences the lithium-ion solvation structure. For further study, *in-situ* FTIR was applied to reveal the interfacial evolution of electrolyte as the SEI formation process at the initial cycle (**Figure 2c, 2d and S8**).[26, 27] It should be noted that the FTIR signals recorded at open circuit voltage (2.5 V) is used as baseline, hence all reverse peaks detected *in-situ* indicate consumption of specific electrolyte components near the electrode surface. As the potential discharging to relatively low potential range, the signals presenting EC (1806 $cm^{-1}$, 1162 $cm^{-1}$), $Li^+$-EC (1770 $cm^{-1}$, 1196 $cm^{-1}$), EMC (1745 $cm^{-1}$, 1265 $cm^{-1}$) and $Li^+$-EMC (1713 $cm^{-1}$, 1308 $cm^{-1}$) exhibit obvious attenuation in BE, indicating the drastic decomposition of organic solvent as the formation of SEI. By contrast, the corresponding decomposition peaks of above-mentioned solvents are dramatically inhibited at the presence of TVSi additive. It is believed that the organic components of SEI derived from the solvent decomposition is unstable, failing to provide enough chemical stabilities and mechanical properties to

accommodate the volume expansion of Si anode.[28] Thanks to the decomposition of TVSi prior to the decomposing potential of solvents (**Figure 1b**), a passivation interphase can be effectively constructed to on the surface of Si anode to inhibit the unlimited decompositions of solvents, contributing to the formation of compact and robust SEI.

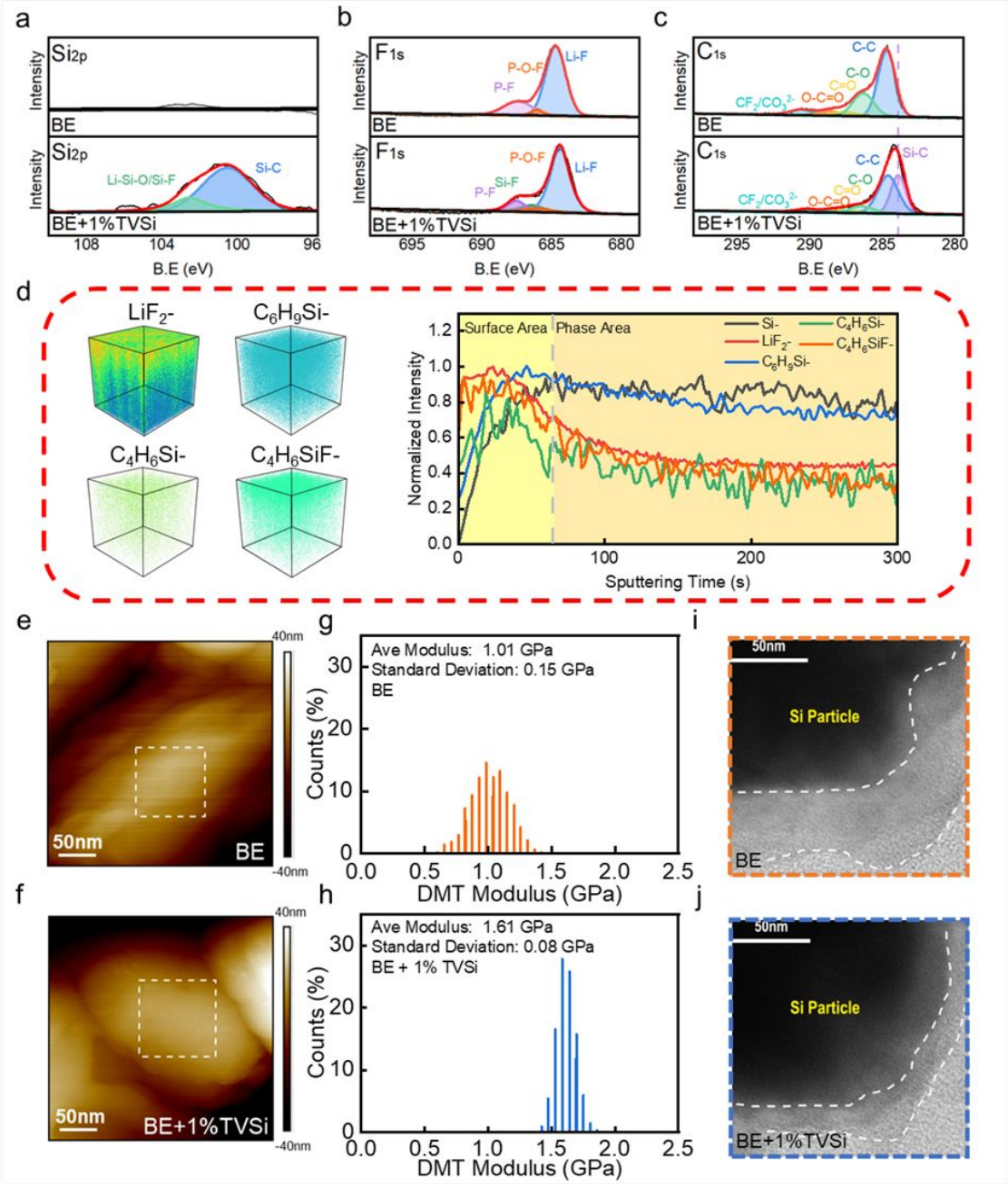


**Figure 3.** SEI characterizations on Si anodes. (a) XPS spectra of Si2p, (b) XPS spectra of F1s and (c) XPS spectra of C1s. (d) TOF-SIMS 3D visualization spectra for Si-, $LiF_2$-, $C_6H_9Si$- and $C_4H_6Si$- debris with BE + 1% TVSi. AFM images (e,f) of the silicon particle with (e) BE and (f) BE + 1% TVSi, and the modulus distribution graphs (g,h) of the SEI derived from them. TEM images of the Si SEI after 200 cycles with (i) BE and (j) BE + 1% TVSi.

X-ray photoelectron spectroscopy (XPS) and time of flight secondary ion mass spectrometry (TOF-SIMs) were carried out to investigate the difference on SEI component and structure. For the Si2p spectra (**Figure 3a, S9**), two new peaks corresponding to Li-Si-O/Si-F (102.5 eV) and Si-C (100.5 eV) appear when 1% TVSi is added, while no peaks can be observed in BE.[29, 30] After etching for 40s, Si-O and Li-Si-O signals begin to appear in the BE group (**Figure S10**). Above results indicate that the Si-containing species detected on the anode surface originated from the decomposition of TVSi while the in-depth signals are attributed to bulk Si. For BE + 1% TVSi, the extra new peak in F1s spectra at 686.4 eV and the new peak at 283.6 eV in C1s spectra confirm the existence of Si-F and Si-C bonding, respectively (**Figure 3b & 3c**).[31, 32] These XPS peaks demonstrate the existence of silane-derived polymer product on Si surface. TOFSIMS results are in agreement with XPS (**Figure 3d**), where both silane polymer fragments and fluorides are detected. From the distribution curves, it can be found that the silane relative fragments have similar distribution tendency as fluorides such as $LiF_2$-. Therefore, it can be speculated that TVSi decomposes simultaneously with FEC on the anode side, forming an inorganic-silane interpenetrating network composite SEI, which is expected to improve the modulus distribution and minimize the stress concentration points.

To verify the above speculation, atomic force microscope (AFM) was employed to measure the mechanical property of SEI on Si. To ensure the measurements reflect the SEI on the silicon anode surface, the nano-Si particle morphologies are firstly detected and the brightest regions with minimum height variations are chosen to measure the modulus (**Figure 3e-f**). As shown in **Figure 3g-h**, the average modulus of the SEI in BE is 1.01 GPa with the standard deviation of 0.15 GPa. In comparison, TVSi results in a higher average modulus of 1.61 GPa and a lower standard deviation of 0.08 GPa, suggesting a harder and more homogeneous SEI. According to the *in-situ* FTIR results, with the addition of TVSi, the decomposition of organic solvents is inhibited, leading to a SEI with desirable mechanical properties that disperse the stress and restrict cracks formation. By contrast, with a higher amount of solvent-derived components, the SEI formed in BE exhibits lower modulus and uniformity, hence unable to tolerate the volume swing of Si.[33] In addition, the observation of microcracks on electrode surface through scanning electron microscope (SEM) agrees with our speculations (**Figure S11**). The transmission electron microscope (TEM) observation results also indicate that a resilient SEI can prevent repeated SEI formation. As shown in **Figure 3i-j**, a thicker SEI is formed in BE compared with that in BE + 1% TVSi. The thick SEI increases the polarization and hinders the migration of lithium-ion, which explain the electrochemical performance obtained in BE.

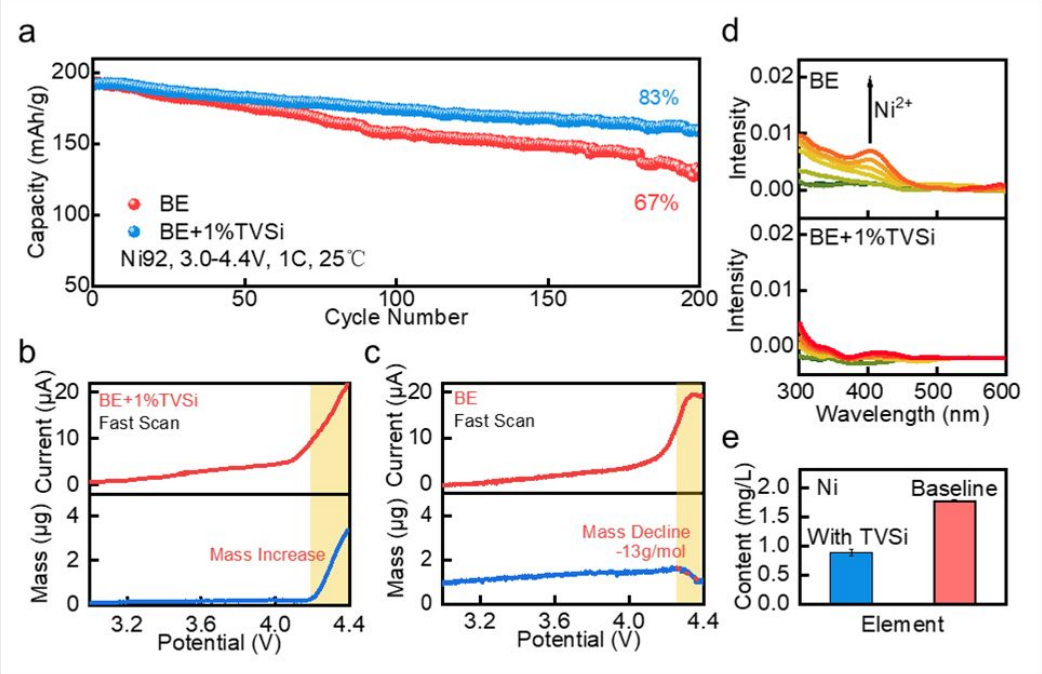


**Figure 4.** (a) Cycle performance at 25℃ of Ni92 half cells with the blank electrolyte and 1% TVSi additive electrolyte. EQCM result: (b) the blank electrolyte and (e) 1% TVSi additive electrolyte. (c) *In-situ* UV-Vis result of the blank electrolyte and 1% TVSi additive electrolyte. (d) ICP result of nickel ion content at the lithium metal anode.

Apart from Si anode, TVSi is also beneficial to Ni92 cathode. As shown in **Figure 4a**, the specific capacity retention can be improved from 67% to 83% after 200 cycles with 1% TVSi. Under elevated temperatures, the improvement becomes more significant (**Figure S12**): TVSi additive enables a capacity retention of 77% after 150 cycles at 45 ℃ while the cell with BE completely fails. Our performance is competitive among currently reported works (**Table S1**). To reveal the protection mechanism, the mass of the cathodes in both electrolytes were *in-situ* measured by electrochemical quartz crystal microbalance (EQCM). As shown in **Figure 4b & 4c**, under high voltages, the mass on Ni92 cathode is detected to decrease in BE, with a mass variated per mole of electron transferring of -13 g $mol^{-1}$, which is higher that of delithiation process (-7 g $mol^{-1}$).[34] As the growth of CEI formation should result in mass increase, the deviation might be due to the TM (mostly Ni) dissolution in BE. By comparison, in the presence of 1% TVSi, great mass increasement is detected at high voltage, which symbolizes the additional oxidation progress of TVSi forming a dense CEI to protect the interface. To further observe the Ni dissolution, *in-situ* ultraviolet-visible spectrum (UV-Vis) is utilized to detect the trace transition metal ion during the cycling (**Figure 4d**). The peak at around 400 nm corresponding to $Ni^{2+}$ signal[35] is more intense in BE than in BE + 1% TVSi, indicating the more severe Ni dissolution without TVSi. Inductively coupled plasma atomic emission spectrometry (ICP AES) was also applied to measure the transition metals deposited on the anode (**Figure 4e**). The anode cycled with TVSi shows lower transition metal content compared with BE, which further confirms the ability of TVSi of supressing the Ni dissolution.

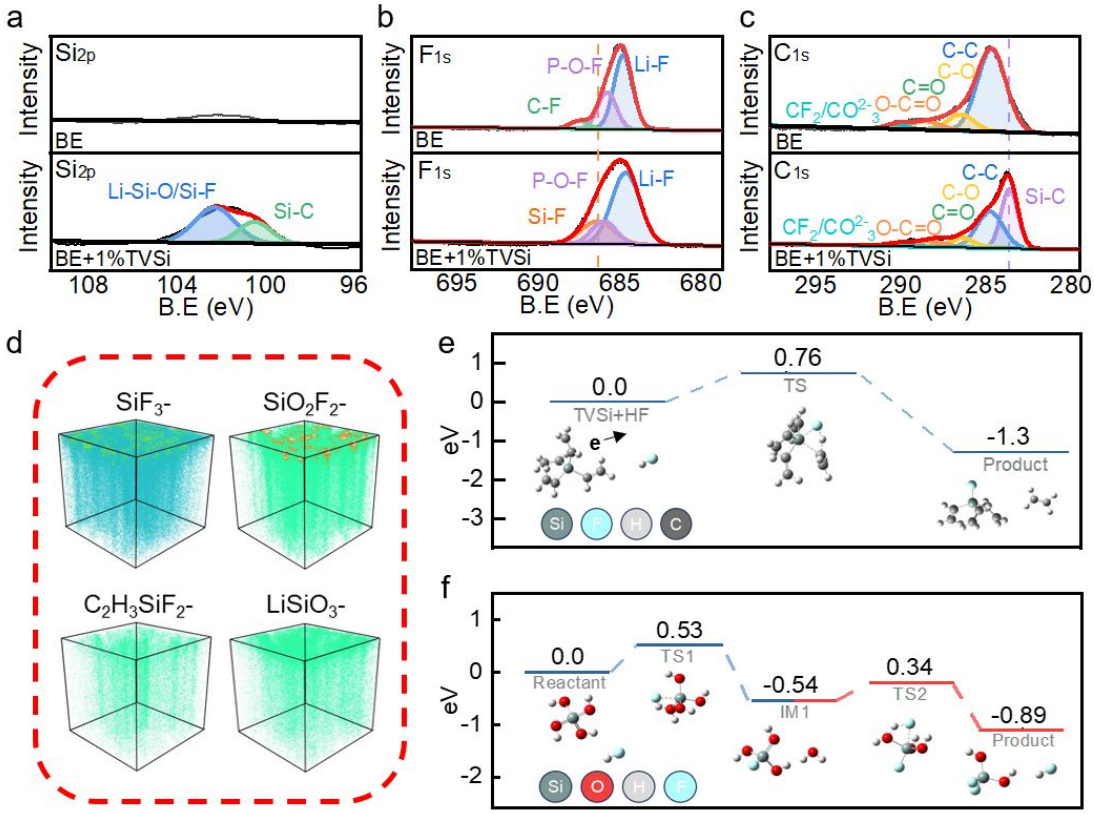


**Figure 5.** Characterization on the CEI chemical components and structure of the Ni92 cathode using the blank electrolyte and 1% TVSi additive electrolyte: (a) XPS spectra of Si 2p, (b) XPS spectra of F 1s, (c) XPS spectra of C 1s. (d) TOFSIMS 3D visualization spectra for $LiSiO_3$-, $SiO_2F_2$-, $SiF_3$- and $C_2H_3SiF_2$- debris with different electrolytes. HF scavenging process of TVSi at cathode: (e) reaction between TVSi and HF, and (f) reaction between silicate and HF.

XPS is then utilized to analyse the components of CEI (**Figure 5a-c**). Compared with BE, two new peaks at 102.5eV and 100.5eV emerge in Si2p spectra with 1% TVSi, corresponding to Li-Si-O/Si-F and Si-C respectively. F1s and C1s spectra also confirm the existence of Si-F and Si-C bonding. The existence of Si-C and Si-O bonds mostly originate from the products of TVSi and the Si-F bond is possibly related to the HF scavenging process. TOFSIMS measurement was performed to further analyse the possible product (**Figure 5d, Figure S13 and S14**). According to the 3D distribution graphs and fragments distribution curve, a wealth of fluorinated fragments such as $SiF_3$-, $SiF_4$- $SiO_2F_2$- and $C_2H_3SiF_2$- can be observed on the surface. These fragments are probably the result of the reaction between silicate (or TVSi) and HF. To verify the mechanism of the HF scavenging process, DFT method calculation is applied to investigate the reaction process (**Figure 5e-f**). HF can be eliminated by reacting with TVSi or (Si-C=C group) via Si-C breaking and Si-F formation with an electron loss. The transition state of the reaction is 0.76 eV higher than the reactant and the energy level of the final product are lower than the reactant, demonstrating the feasibility of the reaction. The silicate in the CEI also plays a role in scavenging the HF. The oxygen is initially coordinated with a hydrogen to

form a hydroxyl group. The hydroxyl group later reacts with HF via a Si-O breaking and Si-F formation. Therefore, during the charge-discharge process, when HF is transferring to the Ni92 cathode, the CEI will capture it before it contacts with the surface lattice, restraining its attack on Ni92 phase and supressing the nickel dissolution. By scavenging the HF, the severe cracks formation in secondary particle is also inhibited. As shown in **Figure S15**, severe cracks are formed in BE, which will further increase the electrolyte contact areas and thus accelerate the electrolyte consumption and structural damage of Ni92.

According to distribution curves of TOFSIMs, in addition to commonly reported inorganic fragments such as $LiF_2$-, inorganic fragments originated from silicate such as $LiSiO_3$-, $LiSiO_4$- are detected concentrating on the top of CEI. The above results suggest that TVSi initially form a polymer layer on the cathode, and later, the silane polymer on the cathode surface is partially oxidized to inorganic products to form an inorganic-silane composite CEI with chemically bonded interfaces, resulting in enhanced rigidity and mechanical strength (Figure **S16**). This compact CEI structure serves as a barrier, preventing the penetration of the electrolyte and thereby reducing the probability of side reactions. Furthermore, the silicate contacting the cathode phase also plays an important role in restraining the side reactions. The much stronger bonding energy of Si-O (798kJ/mol) than TM-O (391.6kJ/mol) drags the oxygen atoms toward Si atoms from Ni atoms, reducing the nickel oxidation valence state.[36] As mostly reported, higher Ni valence has the higher catalytic activity that induces serious side reaction, which not only leads to the consumption of electrolyte but also accelerate the cation mixing causing the irreversible phase transition.[37-39] Therefore, the compact and functional CEI is expected to restrain the rock-salt phase transition. TEM results (**Figure S17**) also show that for the Ni92 cathode cycled in BE, a large rock-salt phase region can be observed, which is not only electrochemically inert, but also obstructive to lithium-ion transfer. By sharp contrast, rock-salt phase can be barely observed in the material cycled in BE + 1% TVSi.

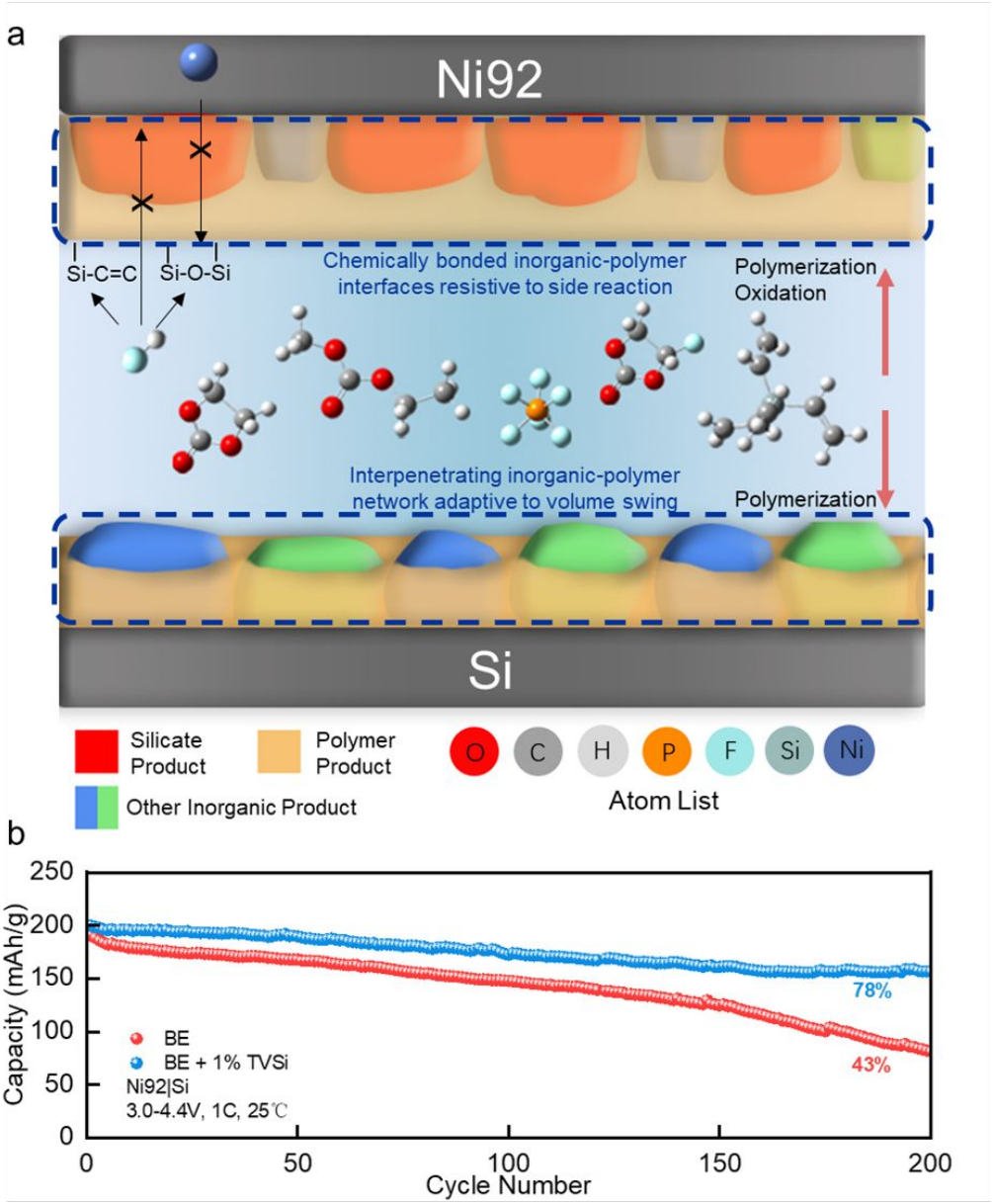


**Figure 6.** (a) Schematic illustration of the protective mechanism of TVSi additive. (a) Electrochemical performance of Ni92-Si(pre-lithiation) full cell.

From the experimental and theoretical results, the function of TVSi can be schematically illustrated in **Figure 6a**. TVSi polymerizes on the electrode and mechanically binds with inorganic components to form a resilient composite SEI, which is capable of accommodating volume changes of Si, suppressing constant electrolyte consumption and SEI growth. At cathode, when HF is attacking the lattice, the Si-C=C and Si-O functional structure on the surface of the cathode can pre-emptively react with it, thereby restricting the Ni dissolution. Additionally, the chemical bonding between inorganic-organic interfaces within CEI inhibits the penetration of the electrolyte, thus reducing the side reactions and hampering the irreversible phase transition. Finally, proof-of-concept full cells consisting of Ni92 cathode and pre-lithiated Si anode were assembled and tested. As shown in **Figure**

**6b & S18**, the specific capacity retention of the full cells can be greatly improved at both 25℃ and 45℃, demonstrating large potentials of TVSi in practical use.

## 4. Conclusion

This work presents a comprehensive investigation into the capacity of tetravinylsilane (TVSi) as an electrolyte additive in lithium-ion batteries, with a particular focus on Si anodes and Ni-rich cathodes. The integration of TVSi significantly bolsters battery stability and performance. In silicon anodes, TVSi enables the formation of an interpenetrating network composite SEI consisting of flexible silane-based polymer embedded with rigid inorganic component. This SEI adeptly accommodate the volume swing of silicon, thereby reducing electrolyte consumption and SEI aging. On the cathode side, TVSi contributes to the formation of an inorganic-silane composite CEI with chemically bonded interfaces. The dense CEI not only curtails the nickel dissolution, but also impedes the electrolyte penetration, inhibits the side reaction and further supresses the irreversible phase transition. Consequently, the dual functionality of TVSi in stabilizing both electrodes lead to notable improvement in full cell. This research paves the way for the development of electrolyte additives capable of constructing tailored SEI and CEI, further advancing battery design.

## Supporting Information

Supporting Information is available and includes supplementary data in this manuscript.

## Conflict of Interest

There is no conflict of interest to report.

## Funding Information

This work was supported by the National Natural Science Foundation of China (52303263), Shenzhen Science and Technology Research grant (JCYJ20200109140416788) and the Soft Science Research Project of Guangdong Province (2017B030301013).

## References


1. Guo, J.; Dong, D.; Wang, J.; Liu, D.; Yu, X.; Zheng, Y.; Wen, Z.; Lei, W.; Deng, Y.; Wang, J.; Hong, G.; Shao, H., Silicon-Based Lithium Ion Battery Systems: State-of-the-Art from Half and Full Cell Viewpoint. *Advanced Functional Materials* **2021,** *31*, 2102546. DOI: 10.1002/adfm.202102546.
2. Ge, M.; Cao, C.; Biesold, G. M.; Sewell, C. D.; Hao, S.-M.; Huang, J.; Zhang, W.; Lai, Y.; Lin, Z., Recent Advances in Silicon-Based Electrodes: From Fundamental Research toward Practical Applications. *Adv. Mater.* **2021,** *33*, 2004577. DOI: 10.1002/adma.202004577.
3. Ryu, H.-H.; Park, K.-J.; Yoon, C. S.; Sun, Y.-K., Capacity Fading of Ni-Rich Li[NixCoyMn1–x–y]O2 ($0.6 \leq x \leq 0.95$) Cathodes for High-Energy-Density Lithium-Ion Batteries: Bulk or Surface Degradation? *Chem. Mater.* **2018,** *30*, 1155-1163. DOI: 10.1021/acs.chemmater.7b05269.
4. Li, W.; Erickson, E. M.; Manthiram, A., High-nickel layered oxide cathodes for lithium-based automotive batteries. *Nat. Energy* **2020,** *5*, 26-34. DOI: 10.1038/s41560-019-0513-0.
5. Wu, H.; Cui, Y., Designing nanostructured Si anodes for high energy lithium ion batteries. *Nano Today* **2012,** *7*, 414-429. DOI: 10.1016/j.nantod.2012.08.004.
6. Qian, G.; Li, Y.; Chen, H.; Xie, L.; Liu, T.; Yang, N.; Song, Y.; Lin, C.; Cheng, J.; Nakashima, N.; Zhang, M.; Li, Z.; Zhao, W.; Yang, X.; Lin, H.; Lu, X.; Yang, L.; Li, H.; Amine, K.; Chen, L.; Pan, F., Revealing the aging process of solid electrolyte interphase on SiOx anode. *Nat. Commun.* **2023,** *14*, 6048. DOI: 10.1038/s41467-023-41867-6.
7. Jin, Y.; Zhu, B.; Lu, Z.; Liu, N.; Zhu, J., Challenges and Recent Progress in the Development of Si Anodes for Lithium-Ion Battery. *Adv. Energy Mater.* **2017,** *7*, 1700715. DOI: 10.1002/aenm.201700715.
8. Etacheri, V.; Haik, O.; Goffer, Y.; Roberts, G. A.; Stefan, I. C.; Fasching, R.; Aurbach, D., Effect of Fluoroethylene Carbonate (FEC) on the Performance and Surface Chemistry of Si-Nanowire Li-Ion Battery Anodes. *Langmuir* **2012,** *28*, 965-976. DOI: 10.1021/la203712s.
9. Markevich, E.; Salitra, G.; Aurbach, D., Fluoroethylene Carbonate as an Important Component for the Formation of an Effective Solid Electrolyte Interphase on Anodes and Cathodes for Advanced Li-Ion Batteries. *ACS Energy Lett.* **2017,** *2*, 1337-1345. DOI: 10.1021/acsenergylett.7b00163.
10. Xu, C.; Lindgren, F.; Philippe, B.; Gorgoi, M.; Björefors, F.; Edström, K.; Gustafsson, T., Improved Performance of the Silicon Anode for Li-Ion Batteries: Understanding the Surface Modification Mechanism of Fluoroethylene Carbonate as an Effective Electrolyte Additive. *Chem. Mater.* **2015,** *27*, 2591-2599. DOI: 10.1021/acs.chemmater.5b00339.
11. Zhu, C.; Chen, S.; Li, K.; Yin, Z.-W.; Xiao, Y.; Lin, H.; Pan, F.; Yang, L., Quantitative analysis of the structural evolution in Si anode via multi-scale image reconstruction. *Sci. Bull.* **2023,** *68*, 408-416. DOI: 10.1016/j.scib.2023.01.032.
12. Chen, J.; Fan, X.; Li, Q.; Yang, H.; Khoshi, M. R.; Xu, Y.; Hwang, S.; Chen, L.; Ji, X.; Yang, C.; He, H.; Wang, C.; Garfunkel, E.; Su, D.; Borodin, O.; Wang, C., Electrolyte design for LiF-rich solid–electrolyte interfaces to enable high-performance microsized alloy anodes for batteries. *Nat. Energy* **2020,** *5*, 386-397. DOI: 10.1038/s41560-020-0601-1.
13. Cao, Z.; Zheng, X.; Qu, Q.; Huang, Y.; Zheng, H., Electrolyte Design Enabling a High-Safety and High-Performance Si Anode with a Tailored Electrode–Electrolyte Interphase. *Adv. Mater.* **2021,** *33*, 2103178. DOI: 10.1002/adma.202103178.
14. Rinkel, B. L. D.; Hall, D. S.; Temprano, I.; Grey, C. P., Electrolyte Oxidation Pathways in

Lithium-Ion Batteries. *Journal of the American Chemical Society* **2020,** *142*, 15058-15074. DOI: 10.1021/jacs.0c06363.

15. Jayawardana, C.; Rodrigo, N.; Parimalam, B.; Lucht, B. L., Role of Electrolyte Oxidation and Difluorophosphoric Acid Generation in Crossover and Capacity Fade in Lithium Ion Batteries. *ACS Energy Lett.* **2021,** *6*, 3788-3792. DOI: 10.1021/acsenergylett.1c01657.

16. Kim, K.; Park, I.; Ha, S.-Y.; Kim, Y.; Woo, M.-H.; Jeong, M.-H.; Shin, W. C.; Ue, M.; Hong, S. Y.; Choi, N.-S., Understanding the thermal instability of fluoroethylene carbonate in LiPF6-based electrolytes for lithium ion batteries. *Electrochim. Acta* **2017,** *225*, 358-368. DOI: 10.1016/j.electacta.2016.12.126.

17. Zhao, X.; Zhuang, Q.-C.; Xu, S.-D.; Xu, Y.-X.; Shi, Y.-L.; Zhang, X.-X., A New Insight into the Content Effect of Fluoroethylene Carbonate as a Film Forming Additive for Lithium-Ion Batteries. *Int. J. Electrochem. Sci.* **2015,** *10*, 2515-2534. DOI: 10.1016/S1452-3981(23)04865-4.

18. Sahore, R.; O'Hanlon, D. C.; Tornheim, A.; Lee, C.-W.; Garcia, J. C.; Iddir, H.; Balasubramanian, M.; Bloom, I., Revisiting the Mechanism Behind Transition-Metal Dissolution from Delithiated LiNixMnyCozO2 (NMC) Cathodes. *J. Electrochem. Soc.* **2020,** *167*, 020513. DOI: 10.1149/1945-7111/ab6826.

19. Zhang, D.; Liu, M.; Ma, J.; Yang, K.; Chen, Z.; Li, K.; Zhang, C.; Wei, Y.; Zhou, M.; Wang, P.; He, Y.; Lv, W.; Yang, Q.-H.; Kang, F.; He, Y.-B., Lithium hexamethyldisilazide as electrolyte additive for efficient cycling of high-voltage non-aqueous lithium metal batteries. *Nat. Commun.* **2022,** *13*, 6966. DOI: 10.1038/s41467-022-34717-4.

20. Chen, Z.; Soltani, A.; Chen, Y.; Zhang, Q.; Davoodi, A.; Hosseinpour, S.; Peukert, W.; Liu, W., Emerging Organic Surface Chemistry for Si Anodes in Lithium-Ion Batteries: Advances, Prospects, and Beyond. *Adv. Energy Mater.* **2022,** *12*, 2200924. DOI: 10.1002/aenm.202200924.

21. Fang, J.-B.; Chang, S.-z.; Ren, Q.; Zi, T.-q.; Wu, D.; Li, A.-D., Tailoring Stress and Ion-Transport Kinetics via a Molecular Layer Deposition-Induced Artificial Solid Electrolyte Interphase for Durable Silicon Composite Anodes. *ACS Appl. Mater. Interfaces* **2021,** *13*, 32520-32530. DOI: 10.1021/acsami.1c07572.

22. Wang, H.; Sun, D.; Li, X.; Ge, W.; Deng, B.; Qu, M.; Peng, G., Alternative Multifunctional Cyclic Organosilicon as an Efficient Electrolyte Additive for High Performance Lithium-Ion Batteries. *Electrochim. Acta* **2017,** *254*, 112-122. DOI: 10.1016/j.electacta.2017.09.111.

23. Dong, Z.; Wei, J.; Yue, H.; Zhang, K.; Wang, L.; Li, X.; Zhang, Z.; Yang, W.; Yang, S., Multifunctional organosilicon compound contributes to stable operation of high-voltage lithium metal batteries. *J. Colloid Interface Sci.* **2021,** *595*, 35-42. DOI: 10.1016/j.jcis.2021.03.058.

24. Han, J.-G.; Jeong, M.-Y.; Kim, K.; Park, C.; Sung, C. H.; Bak, D. W.; Kim, K. H.; Jeong, K.-M.; Choi, N.-S., An electrolyte additive capable of scavenging HF and PF5 enables fast charging of lithium-ion batteries in LiPF6-based electrolytes. *J. Power Sources* **2020,** *446*, 227366. DOI: 10.1016/j.jpowsour.2019.227366.

25. Haridas, A. K.; Nguyen, Q. A.; Terlier, T.; Blaser, R.; Biswal, S. L., Investigating the Compatibility of TTMSP and FEC Electrolyte Additives for LiNi0.5Mn0.3Co0.2O2 (NMC)–Silicon Lithium-Ion Batteries. *ACS Appl. Mater. Interfaces* **2021,** *13*, 2662-2673. DOI: 10.1021/acsami.0c19347.

26. Zhang, Y.; Katayama, Y.; Tatara, R.; Giordano, L.; Yu, Y.; Fraggedakis, D.; Sun, J. G.; Maglia, F.; Jung, R.; Bazant, M. Z.; Shao-Horn, Y., Revealing electrolyte oxidation via carbonate dehydrogenation on Ni-based oxides in Li-ion batteries by in situ Fourier transform infrared

spectroscopy. *Energy Environ. Sci.* **2020,** *13*, 183-199. DOI: 10.1039/C9EE02543J.
27. Yan, Y.; Weng, S.; Fu, A.; Zhang, H.; Chen, J.; Zheng, Q.; Zhang, B.; Zhou, S.; Yan, H.; Wang, C.-W.; Tang, Y.; Luo, H.; Mao, B.-W.; Zheng, J.; Wang, X.; Qiao, Y.; Yang, Y.; Sun, S.-G., Tailoring Electrolyte Dehydrogenation with Trace Additives: Stabilizing the LiCoO2 Cathode beyond 4.6 V. *ACS Energy Lett.* **2022,** *7*, 2677-2684. DOI: 10.1021/acsenergylett.2c01433.
28. Ji, Y.; Qiu, J.; Zhao, W.; Liu, T.; Dong, Z.; Yang, K.; Zheng, G.; Qian, G.; Yang, M.; Chen, Q.; Amine, K.; Pan, F.; Yang, L., In situ probing the origin of interfacial instability of Na metal anode. *Chem* **2023,** *9*, 2943-2955. DOI: 10.1016/j.chempr.2023.06.002.
29. Sun, C.; Wang, Y.-J.; Gu, H.; Fan, H.; Yang, G.; Ignaszak, A.; Tang, X.; Liu, D.; Zhang, J., Interfacial coupled design of epitaxial Graphene@SiC Schottky junction with built-in electric field for high-performance anodes of lithium ion batteries. *Nano Energy* **2020,** *77*, 105092. DOI: 10.1016/j.nanoen.2020.105092.
30. Huang, D.; Yin, L.; Niu, J., Photoinduced Hydrodefluorination Mechanisms of Perfluorooctanoic Acid by the SiC/Graphene Catalyst. *Environ. Sci. Technol.* **2016,** *50*, 5857-5863. DOI: 10.1021/acs.est.6b00652.
31. Brunet, M.; Aureau, D.; Chantraine, P.; Guillemot, F.; Etcheberry, A.; Gouget-Laemmel, A. C.; Ozanam, F., Etching and Chemical Control of the Silicon Nitride Surface. *ACS Appl. Mater. Interfaces* **2017,** *9*, 3075-3084. DOI: 10.1021/acsami.6b12880.
32. Aupperle, F.; Eshetu, G. G.; Eberman, K. W.; Xioa, A.; Bridel, J.-S.; Figgemeier, E., Realizing a high-performance LiNi0.6Mn0.2Co0.2O2/silicon–graphite full lithium ion battery cell via a designer electrolyte additive. *J. Mater. Chem. A* **2020,** *8*, 19573-19587. DOI: 10.1039/D0TA05827K.
33. Zhao, Q.; Stalin, S.; Archer, L. A., Stabilizing metal battery anodes through the design of solid electrolyte interphases. *Joule* **2021,** *5*, 1119-1142. DOI: 10.1016/j.joule.2021.03.024.
34. Ji, Y.; Yin, Z.-W.; Yang, Z.; Deng, Y.-P.; Chen, H.; Lin, C.; Yang, L.; Yang, K.; Zhang, M.; Xiao, Q.; Li, J.-T.; Chen, Z.; Sun, S.-G.; Pan, F., From bulk to interface: electrochemical phenomena and mechanism studies in batteries via electrochemical quartz crystal microbalance. *Chem. Soc. Rev.* **2021,** *50*, 10743-10763. DOI: 10.1039/D1CS00629K.
35. Jin, B.; Cui, Z.; Manthiram, A., In situ Interweaved Binder Framework Mitigating the Structural and Interphasial Degradations of High-nickel Cathodes in Lithium-ion Batteries. *Angew. Chem. Int. Ed.* **2023,** *62*, e202301241. DOI: 10.1002/anie.202301241.
36. Jiang, Y.; Bi, Y.; Liu, M.; Peng, Z.; Huai, L.; Dong, P.; Duan, J.; Chen, Z.; Li, X.; Wang, D.; Zhang, Y., Improved stability of Ni-rich cathode by the substitutive cations with stronger bonds. *Electrochim. Acta* **2018,** *268*, 41-48. DOI: 10.1016/j.electacta.2018.01.119.
37. Jiang, M.; Danilov, D. L.; Eichel, R.-A.; Notten, P. H. L., A Review of Degradation Mechanisms and Recent Achievements for Ni-Rich Cathode-Based Li-Ion Batteries. *Adv. Energy Mater.* **2021,** *11*, 2103005. DOI: 10.1002/aenm.202103005.
38. Kim, U.-H.; Ryu, H.-H.; Kim, J.-H.; Mücke, R.; Kaghazchi, P.; Yoon, C. S.; Sun, Y.-K., Microstructure-Controlled Ni-Rich Cathode Material by Microscale Compositional Partition for Next-Generation Electric Vehicles. *Adv. Energy Mater.* **2019,** *9*, 1803902. DOI: 10.1002/aenm.201803902.
39. Park, N.-Y.; Park, G.-T.; Kim, S.-B.; Jung, W.; Park, B.-C.; Sun, Y.-K., Degradation Mechanism of Ni-Rich Cathode Materials: Focusing on Particle Interior. *ACS Energy Lett.* **2022,** *7*, 2362-2369. DOI: 10.1021/acsenergylett.2c01272.

## Table of Contents Graphic